University of Hertfordshire UH

Citation for the published version:

Lisogorskyi, M., Jones, H., & Feng, F. (2019). Activity and telluric contamination in HARPS observations of Alpha Centauri B. Monthly Notices of the Royal Astronomical Society, *485*(4), 4804–4816. DOI: 10.1093/mnras/stz694

Document Version: Accepted Version

Link to the final published version available at the publisher:

https://doi.org/10.1093/mnras/stz694

This article has been accepted for publication in Monthly Notices of the Royal Astronomical Society. © 2019 The Author(s). Published by Oxford University Press on behalf of the Royal Astronomical Society. All rights reserved.

General rights

Copyright© and Moral Rights for the publications made accessible on this site are retained by the individual authors and/or other copyright owners.

Please check the manuscript for details of any other licences that may have been applied and it is a condition of accessing publications that users recognise and abide by the legal requirements associated with these rights. You may not engage in further distribution of the material for any profitmaking activities or any commercial gain. You may freely distribute both the url (http://uhra.herts.ac.uk/) and the content of this paper for research or private study, educational, or not-for-profit purposes without prior permission or charge.

Take down policy

If you believe that this document breaches copyright please contact us providing details, any such items will be temporarily removed from the repository pending investigation.

Enquiries

Please contact University of Hertfordshire Research & Scholarly Communications for any enquiries at rsc@herts.ac.uk

Monthly Notices
of the
ROYAL ASTRONOMICAL SOCIETY

MNRAS **485,** 4804–4816 (2019)
Advance Access publication 2019 March 27

doi:10.1093/mnras/stz694

Activity and telluric contamination in HARPS observations of Alpha Centauri B

M. Lisogorskyi ,★ H. R. A. Jones and F. Feng
Centre for Astrophysics Research, University of Hertfordshire, College Lane, AL10 9AB Hatfield, UK

Accepted 2019 February 24. Received 2019 January 30; in original form 2018 December 11

ABSTRACT

The Alpha Centauri system is the primary target for planet search as it is the closest star system composed of a solar twin α Cen A, a K-dwarf α Cen B, and an M-dwarf Proxima Centauri, which has a confirmed planet in the temperate zone. α Cen A and B were monitored intensively with the HARPS spectrograph for over 10 yr, providing high-precision radial velocity (RV) measurements. In this work, we study the available data to better understand the stellar activity and other contaminating signals. We highlight the importance of telluric contamination and its impact on the RV measurements. Our suggested procedures lead to discarding about 5 per cent of HARPS data, providing a data set with an rms improved by a factor of 2. We compile and quantify the behaviour of 345 spectral lines with a wide range of line shapes and sensitivity to activity.

Key words: planets and satellites: detection – techniques: radial velocities – stars: activity – stars: individual: HD128621.

1 INTRODUCTION

The first planetary system was confirmed around the pulsar PSR B1257+12 (Wolszczan & Frail 1992) and the first exoplanet orbiting a solar-type star 51 Pegasi was detected three years later (Mayor & Queloz 1995). Today, there are thousands and the number is growing.

The radial velocity (RV) method is currently responsible for detection or confirmation of widest range of exoplanets possible. This method was proposed years before spectrographs with precision high enough to detect planets became available (Struve 1952), with the exception of hot Jupiters. It is an indirect method that measures the motion of the host star around the barycentre of the star–planet system. It relies on tiny shifts in narrow absorption features in stellar spectra, which are prone to variations due to stellar sources of noise such as oscillations, granulation, rotating active regions, and magnetic cycles. The first two can be minimized using an optimized observational strategy (O'Toole, Tinney & Jones 2008), while others have much longer time-scales and can produce periodic signals in RV measurements via line profile variations (e.g. Saar & Donahue 1997; Queloz et al. 2001; Huélamo et al. 2008). Others can be identified and corrected for using activity indicators and cross-correlation function (CCF) asymmetry (e.g. Santos et al. 2001; Lindegren & Dravins 2003; Kürster et al. 2003; Santos et al. 2010). These stellar noise sources already have higher RV amplitude than instrumental noise in high-precision spectrographs like HARPS (Mayor et al. 2003), so a better understanding of the impact of activity on the spectra and RV measurements is required. More recent approaches include analysis of differential RVs (Feng et al. 2017), wavelength-dependent noise via measuring RV from individual spectral lines (Dumusque 2018), and analysis of line shape variations (Davis et al. 2017; Thompson et al. 2017; Wise et al. 2018).

In this work, we analyse the available observations of α Cen system with HARPS and quantify effect of telluric lines and activity-sensitive lines across the whole spectrum. Our focus is on α Cen B (spectral type K1V) due to a large number of observations which are well spaced in time. A weak signal was detected in the system before (Dumusque et al. 2012), but it was not confirmed (Hatzes 2013; Rajpaul, Aigrain & Roberts 2016). Nevertheless, the star still may have low-mass planets (Zhao et al. 2018).

The available data, as well as its quality and rejection criteria, are discussed in Section 2. Telluric contamination is estimated and additional observations are rejected in Section 3. Activity-sensitive lines and a list of indices are discussed in Section 4.

2 DATA

The data set consists of 22 559 high-resolution ($R = 110\,000$) spectra obtained with the HARPS spectrograph between 2005 and 2016, including both α Cen A and B observations. We use the one-dimensional (so called s1d) spectra and RVs produced by the HARPS DRS (Data Reduction Software).

As the stars are very bright, most spectra have signal-to-noise ratio (S/N) above 100. The data are naturally divided into observing seasons (one per year) due to observability of the stars.

★ E-mail: m.lisogorskyi@herts.ac.uk

© 2019 The Author(s)
Published by Oxford University Press on behalf of the Royal Astronomical Society

Downloaded from https://academic.oup.com/mnras/article-abstract/485/4/4804/5420427 by University of Hertfordshire user on 16 May 2019

Despite high S/N on average, some spectra suffer from noise, overexposure, high activity, tellurics or light contamination from the second component of the binary system. Several methods, as well as visual inspection of the spectra, were employed to minimize the noise.

The analysis is focused on α Cen B as it has much better time coverage. Almost all of α Cen A data were taken during five nights in 2005 April and coverage of further seasons is very sparse. The two components are distinguished using equivalent widths (EWs) of Na D doublet (see Section 2.1).

The data in this work include unbinned observations from seasons considered in Dumusque et al. (2012) with addition of later observations.

High cadence observations in 2013 were excluded from this analysis as most measurements from the spectra (like RV and spectral indices) correlate closely with airmass. We expect that a combination of two factors are the cause: light contamination from α Cen A (Bergmann et al. 2015) and point spread function variations over a night (Berdiñas et al. 2016, 2017). These observations should be analysed separately.

2.1 Visual inspection of the spectra

Na D doublet region of the spectrum was visually inspected and classified. In total 249 spectra were rejected – 67 observations removed due to low S/N, 37 due to steep slope of the continuum (change of flux by a factor of 2 within 10 Å), and 58 due to overexposure.

The rejected spectra are shown in Fig. 1, showing data distribution in Na D lines EWs and CCF properties. Most rejected observations are outliers in both plots. Spectra were identified as 'low S/N' if the noise had amplitude of the shallow absorption features in that spectral region (most spectra do not show any clearly visible noise). The limit is to CCF noise of 0.0006 or S/N of 18 in the order 40 (as provided in FITS headers). Overeposed spectra show 'steppy' continuum and very narrow sodium lines, as well as steep slope of the continuum, which most likely comes from the wavelength dependence of non-linear regime of the CCD (Anglada-Escudé & Butler 2012).

The two components of the binary are well separated on the left-hand plot (Fig. 1a) after the bad observations are removed. All spectra with an EW of Na D line at 5889.95Å below 0.8 were identified as α Cen A (4770 spectra), and the ones above – as α Cen B (17 096 spectra). The right-hand plot (Fig. 1b) shows three distinct features – α Cen B CCF computed with K5 template mask, α Cen A CCF computed with G2 template mask, and α Cen A CCF computed with K5 template mask (wrong template mask – about 10 per cent of α Cen A observations affected).

Table 1. Number of observations removed using different proxies. First four rows – outliers due to light contamination removed using spectral indices and CCF, as described in Section 2.2. Last row – limit on telluric contamination using a water line at 6544 Å, as described in Section 3.2. The final list of observations used is available as a supplementary online table.

Proxy	Observations removed	Observations removed by other proxies
Hα	111	0
Na D	73	19
Ca H&K	23	0
$V_{\rm span}$	20	3
EW(6544 Å) > 0.03	616	6

2.2 CCF properties and spectral indices of α Cen B

In this section, the observing seasons were considered separately and the outliers in the spectral indices and CCF properties were removed based on a visual inspection. Observations were considered outliers if the values were more than 3σ for the particular night or season. As a result, 205 observations were removed from the sample (see Table 1).

EWs were calculated as

$$\mathrm{EW} = (\lambda_1 - \lambda_0) - \sum_i \frac{F_{\rm i}}{F_0}\Delta\lambda, \quad (1)$$

where $[\lambda_0–\lambda_1]$ is the range with the core of the line, $F_{\rm i}$ is flux in a data point, F_0 is continuum level, and $\Delta\lambda$ is resolution of the spectrum (0.01Å for all 1D spectra produced by the HARPS DRS). The continuum level is calculated by averaging flux in pre-defined wavelength ranges with few spectral lines on either side of the line core. Line strengths were calculated from fitting a Gaussian function

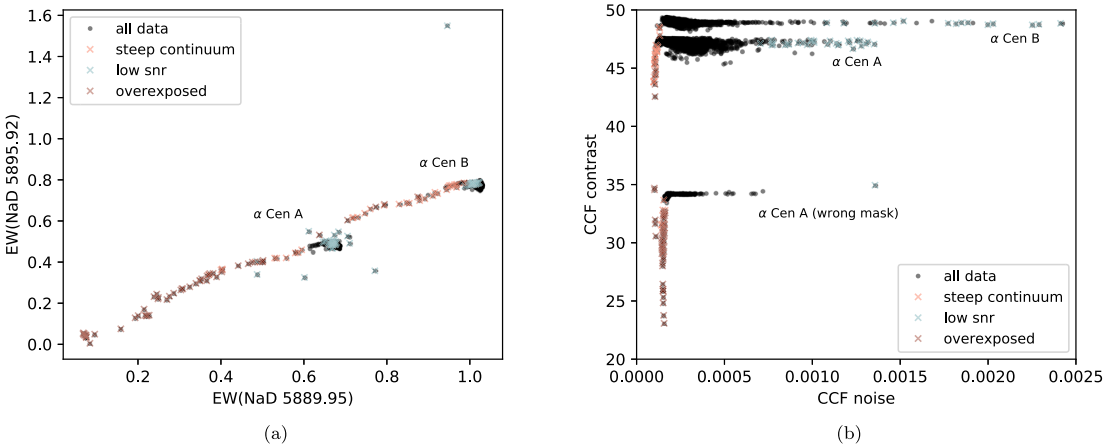

Figure 1. Rejected observations based on visual inspection of the spectra. Black points are all observations available, 'x' show rejected observations due to continuum slope, low S/N, and overexposure. Left: EWs of Na D doublet. Right: CCF contrast versus noise.

Downloaded from https://academic.oup.com/mnras/article-abstract/485/4/4804/5420427 by University of Hertfordshire user on 16 May 2019

to the line as $-A/F_0$, where A is the height of the Gaussian and F_0 is the base.

The EW of Hα was measured at [6561.85–6563.85] Å with continuum measured from [6550.00–6555.00] and [6565.00–6570.00] Å. Line strength, sigma (from Gaussian fit to the line), and EW of H_α were inspected as both methods quantify changes in the same line and only the outliers in both were removed. In total, 111 observations were discarded (∼0.7 per cent of the data).

EWs of Na D lines were measured at 5889.92 and 5895.92 Å with a bandpass of 1 Å. The continuum was estimated from [5800.00–5810.00] and [6080.00–6100.00] Å by averaging the top 10 values from each region (the same spectral ranges as used in Gomes da Silva et al. 2011, but here the lines are measured separately, as described above). The lines were also fitted using four Gaussians – two wide and two narrow components. EWs of both lines were investigated as well as Gaussian parameters of the wide components (which correlate closely with the narrow ones). In total, 54 outliers were discarded.

Mount–Wilson S-index was measured as $S = \alpha \frac{F_H + F_K}{F_R + F_V}$, where F_H is flux measured with triangular filter, centred at 3968.470 Å and with FWHM = 1.09, F_K is flux measured with triangular filter, centred at 3933.664 Å and with FWHM = 1.09, F_R is flux measured in [3891, 3911] Å, F_V is flux measured in [3991, 4011] Å, and α is a constant of proportionality adopted to be 2.4 (Duncan et al. 1991). The value is not corrected for bolometric luminosity. S-index was inspected using the same procedure and 23 outliers were discarded.

The CCF asymmetry was measured as V_{span} – a difference in RV between upper and lower parts of a CCF by fitting a Gaussian. The upper part of the CCF is defined in the range $[-\infty: -1\sigma][+1\sigma: +\infty]$ and the lower part is defined in the range given by $[-\infty: -3\sigma][-1\sigma: +1\sigma][+3\sigma: +\infty]$ (Boisse et al. 2011). V_{span}, CCF FWHM, and CCF contrast were inspected and 17 outliers were removed.

3 TELLURIC CONTAMINATION

Telluric contamination can have a large impact on RV measurements via both deep (Artigau et al. 2014) and shallow (Cunha et al. 2014) absorption features. We selected a pair of deep water lines to estimate the telluric contamination in RV and provide useful practical limits.

3.1 Method

Measuring telluric contamination is quite challenging due to blending of the telluric lines with different atomic lines over the course of a year. The water line at 6543.9 Å was chosen as a proxy for contamination as it is relatively deep and there are no strong atomic features present in its vicinity.

The centroid of the line was estimated to have a width of 0.1 Å, but as a barycentric correction was already applied to the spectra, the line centre moves relative to the stellar spectrum. Its position was empirically approximated with $0.467 \cdot \sin(\frac{2\pi(\mathrm{BJD}-2453693.43)}{364.8}) + 6543.92$. The pseudo-continuum was determined by fitting a second-order polynomial to three regions with no significant line absorption – [6538.5–6540.5], [6544.8–6545.2], and [6556.6–6557.2] Å.

To estimate the error, we measured another, neighbouring water line at 6548.617 Å, which is about twice as weak and blends with slightly stronger atomic lines.

An atomic line template spectrum was produced by averaging RV-corrected spectra with EW(6543.9Å) < 0.002 [all with relative humidity (RH) under 10 per cent]. The telluric lines are virtually non-existent in the selected spectra and so although they have different positions from observation to observation due to the Earth's motion around the Sun they mostly disappear during the averaging. The template and all the observations were corrected for continua using the pseudo-continuum determination described above and the template was subtracted from the observations for further measurement of the remaining telluric lines.

An example spectrum is shown on Fig. 2(a). The atomic template is plotted in red, an example high humidity spectrum is plotted in blue (HARPS.2011-03-03T06:52:24.740, EW(6543.9) = 0.054). The shaded regions show the lines measured, with the width corresponding to the window used to calculate the EW. In the case shown, telluric lines are comparable in depth with narrow absorption features (i.e. the FeI line in the centre of the spectral region), which are crucial for the RV measurements.

The two lines correlate very well with each other (Pearson's $p = 0.96$) and the standard deviation is only 0.0014 Å (see Fig. 2b). The duality in the measurement is correlated with the time of year (telluric lines moving relative to the stellar lines), but does not produce a large error. The offset is produced by the water line at 6543.9Å blending with a shallow Si I feature at 6543.89Å.

3.2 Results

The impact of telluric contamination on RV measurements was evaluated by subtracting the binary component (third-order polynomial fit) from the RV measured from each échelle order and plotting it against the EW of the water line (see Fig. 3a). The data were binned by the number of points – 100 bins, each containing 167 points. The RV values on the figure were brought to the same reference point by subtracting mean RV at low humidity (EW < 0.02). At low telluric contamination, the orders agree reasonably well, but beyond EW > 0.03 some of them start to diverge from the general trend.

The orders that were found to be impacted by tellurics are plotted as solid lines. This disagreement between RV measurements from different orders was quantified in Fig. 3(b) as a standard deviation. This plot shows two trends – one including all the orders and one with most contaminated orders excluded.

One should keep in mind that the RV data contain a sum of all RV signals in addition to telluric contamination (e.g. activity, rotation, companions, etc.). The threshold of EW > 0.03 was chosen as the standard deviation of the RV rapidly increases after this point to twice the value at zero contamination and lowering the threshold does not produce a significant improvement.

The red orders tend to have higher RV scatter with increasing telluric contamination, whereas blue orders tend to do the opposite. This is quantified by échelle order in Fig. 4 (top) as a difference of RVs in the last three bins (high telluric contamination) and low telluric contamination. The vertical lines mark the most contaminated orders. This agrees approximately with the finding of Wright et al. (2016), who found orders 56–59, 63, 64, 66–68, and 71 too contaminated to be used by their RV extraction method.

Again, as these data contain other signals apart from telluric contamination, we compare to the bottom plot on Fig. 4, which shows an RV effect of activity (as measured by log S), using the same binning. Similarly, orders 3–5 show an RV offset, which means that it most likely arises from activity rather than telluric contamination.

Downloaded from https://academic.oup.com/mnras/article-abstract/485/4/4804/5420427 by University of Hertfordshire user on 16 May 2019

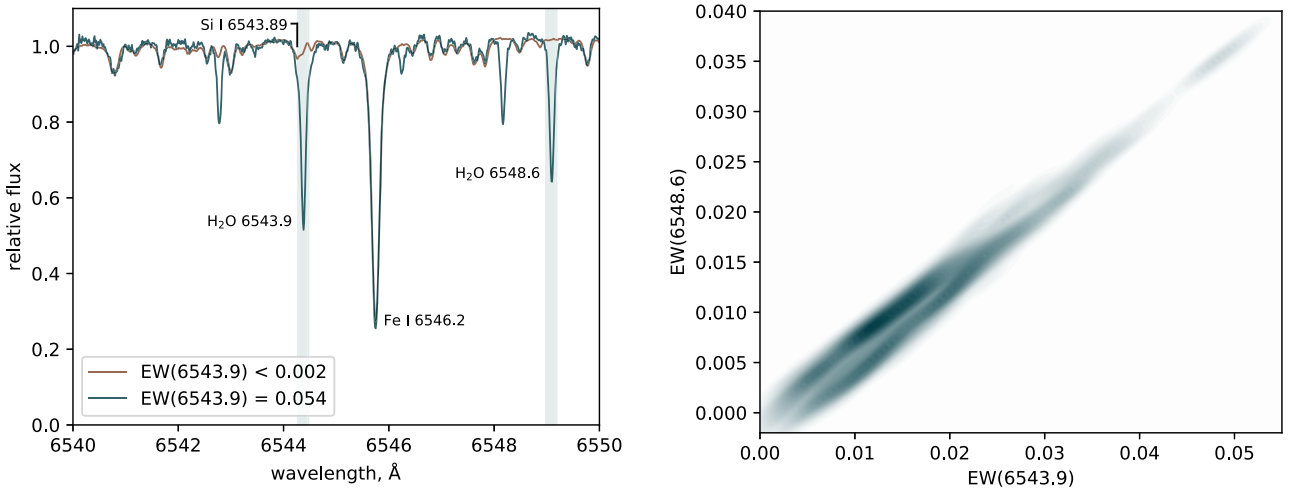

(a) (b)

Figure 2. (a) Spectral region where the water lines were measured. The atomic line template spectrum is plotted in red, a high humidity spectrum (HARPS.2011-03-03T06:52:24.740, EW(6543.9) = 0.054) is in blue. The shaded regions show the lines measured, with the width corresponding to the window used to calculate the EW. The wavelengths of the marked lines are in rest frame, unlike the measured spectra. Comparison plot of the EWs of the two water lines is shown on the right (b) as a density plot.

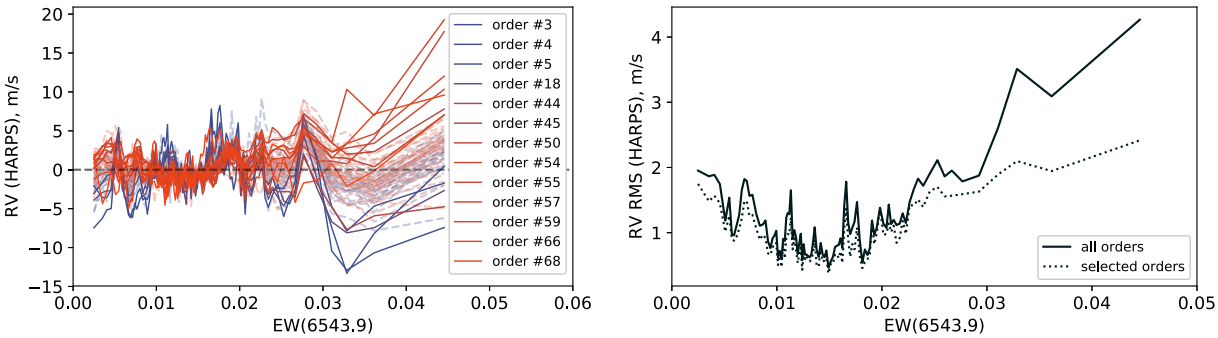

(a) (b)

Figure 3. RV measurements versus telluric contamination measured as EW of a water line at 6543.9 Å. The data are binned by number of points (167 in each bin). Left-hand plot (a) shows RV measured from each échelle order (colour coded appropriately) versus telluric contamination. The orders that were found to be impacted by tellurics are plotted as solid lines. Right-hand plot (b) shows standard deviation as a measure of disagreement between RV measurements from different échelle orders. Solid line includes all 72 orders, and dotted line includes only those identified as less affected by tellurics.

This effect can be avoided by excluding the most impacted orders from RV measurements or rejecting all spectra with EW(6543.9Å) > 0.03Å, which is 616 spectra in this data set. All cuts with numbers of observations rejected are listed in Table 1.

One can estimate the telluric contamination of the RV measurements using the conditions measured at the site. The humidity at La Silla is measured at the meteo station using a thin-film polymer humicap at an altitude of 2 m, as described at the La Silla website.[1] Comparison of telluric contamination as measured by EW(6543.9Å) and the onsite humidity and temperature measurements recorded is shown on Fig. 5. The values of the humidity, temperature, and airmass used were given in FITS headers, apart from 4274 observations in the sample, which have default RH value of 12 per cent. The spectral line measures amount of water vapour along a line of site, so we computed precipitable water vapour (PWV) value using an empirical relationship from Hussain (1984):

$$\mathrm{PWV} = \mathrm{RH}(4.7923 + 0.364T + 0.0055T^2 + 0.0003T^3), \quad (2)$$

where RH is relative humidity and T is temperature in °C.

Here, we assume a linear correlation between the sensor readings and the water line depth, so the figure shows two least-squares line fits – one with an offset (solid line) and one starting at origin (dashed line). The latter represents the assumption of no water line in the spectrum at zero PWV. The two lines have different slopes, but are still quite close to each other. Although the two values closely correlate, Pearson's correlation coefficient is only 0.66. The large scatter around the fits is due to the fact that PWV is calculated using sensors at the observatory site, whereas EW of the water lines measures amount of water along the line of sight. Presumably, low haze or a thin cloud in a particular direction introduces discrepancy in the measurements.

[1] http://www.ls.eso.org/lasilla/dimm/dimm.html

Downloaded from https://academic.oup.com/mnras/article-abstract/485/4/4804/5420427 by University of Hertfordshire user on 16 May 2019

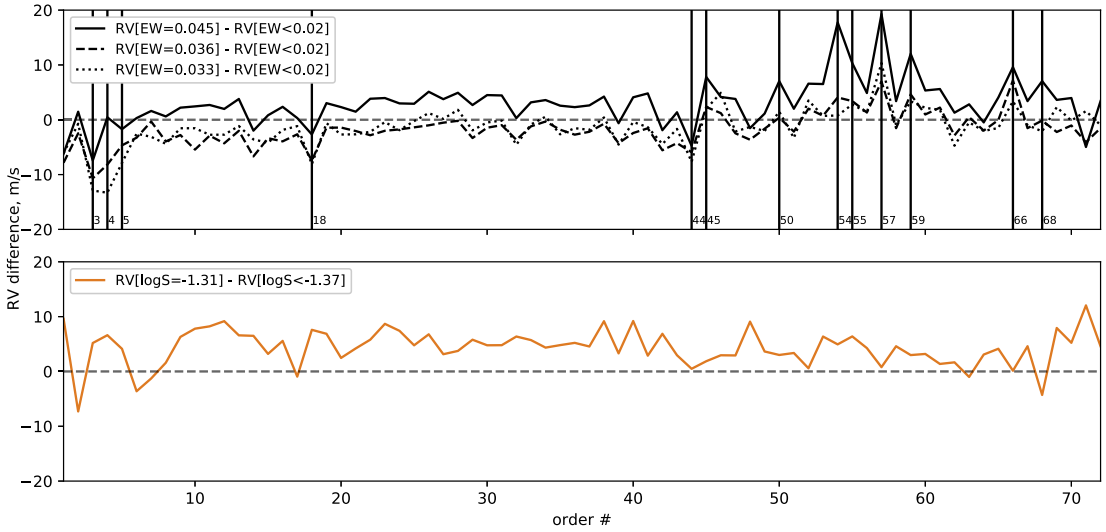

Figure 4. Top: the difference between average RV at high telluric contamination (using last three bins, see Fig. 3a) and low telluric contamination (EW < 0.02) for each échelle order. The orders marked with vertical lines were identified to be affected by telluric contamination the most. Bottom: similar to the top plot, but the difference between average RV at high activity (log $S = -1.31$) and low activity (log $S < -1.37$).

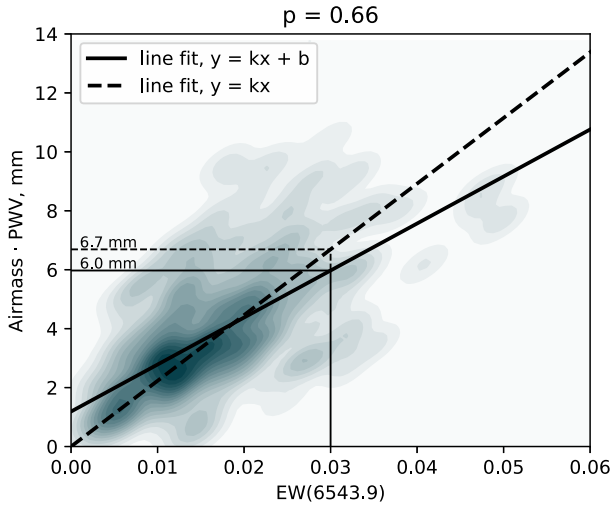

Figure 5. Telluric contamination measured as EW of the water line at 6543.9Å versus airmass-corrected PWV as a density plot. Two line fits are shown in black – one with an offset (solid line) and one starting at origin (dashed line).

If we want to remove the most contaminated observations having only the humidity and temperature information provided in the FITS headers, we will need to assume that these fits are good. This gives us two limits on airmass-corrected PWV – 6.7 and 6.0 mm, as marked on Fig. 5. This way, only 45 per cent or 58 per cent of the contaminated data will be removed, respectively. In addition, 4 per cent or 8 per cent extra (uncontaminated) observations are removed if the PWV condition is applied.

Measuring water vapour from the spectra is more robust, as it represents an actual amount of contamination between a target and a telescope. Removing observations based of the sensor data will result in more contaminated observations left in the data set due to the scatter.

616 observations of α Cen B (3.6 per cent of the data) in our sample have EW(6543.9Å) > 0.03Å and were removed from the analysis, providing a cleaner data set. To quantify, we subtracted binary component from the RV and computed a root mean square:

(i) all data: 5.91 m s^{-1},
(ii) 2013 excluded: 3.45 m s^{-1},
(iii) cleaned data set: 3.08 m s^{-1}.

The rms value is lower compared to the original data set as we removed outliers using multiple proxies (CCF properties, spectral indices, and tellurics), as opposed to just the RV measurements (Zhao et al. 2018).

4 ACTIVITY INDICATORS

α Cen B is a moderately active K-dwarf with log $R'_{\rm HK} = -4.9$ (Henry & Newsom 1996; Dumusque et al. 2012), but still quite a bit of variation is observed. The most commonly used indicator of chromospheric activity is the S-index – measuring emission in cores of the H and K lines of the Ca II (Wilson 1978). HARPS spectra are high resolution and there are enough data available for α Cen B to investigate changes in narrow lines across the whole spectrum. Three features were identified in a small spectral range [4340Å, 4480Å] by Thompson et al. (2017). A strong correlation with Ca II H&K lines was found for one narrow and two wide features: Fe I 4375Å, Fe I 4383Å, and Fe I 4404Å. Another 40 were identified across the whole available spectral range by Wise et al. (2018) using an automated pipeline.

Here, we consider the same season (year 2010) as in Thompson et al. (2017), which has clear rotational activity variations and amplitude comparable to long-term activity. The regular spacing of the observations, sinusoidal variations of the S-index with a relatively high amplitude provide both good sampling and baseline for the activity variations.

4.1 Method

For each observation from 2010 the spectra were corrected for RV (as measured with the HARPS pipeline) and divided by a low activity template. The low activity template was computed by median stacking the 10 spectra with lowest values of S-index.

Downloaded from https://academic.oup.com/mnras/article-abstract/485/4/4804/5420427 by University of Hertfordshire user on 16 May 2019

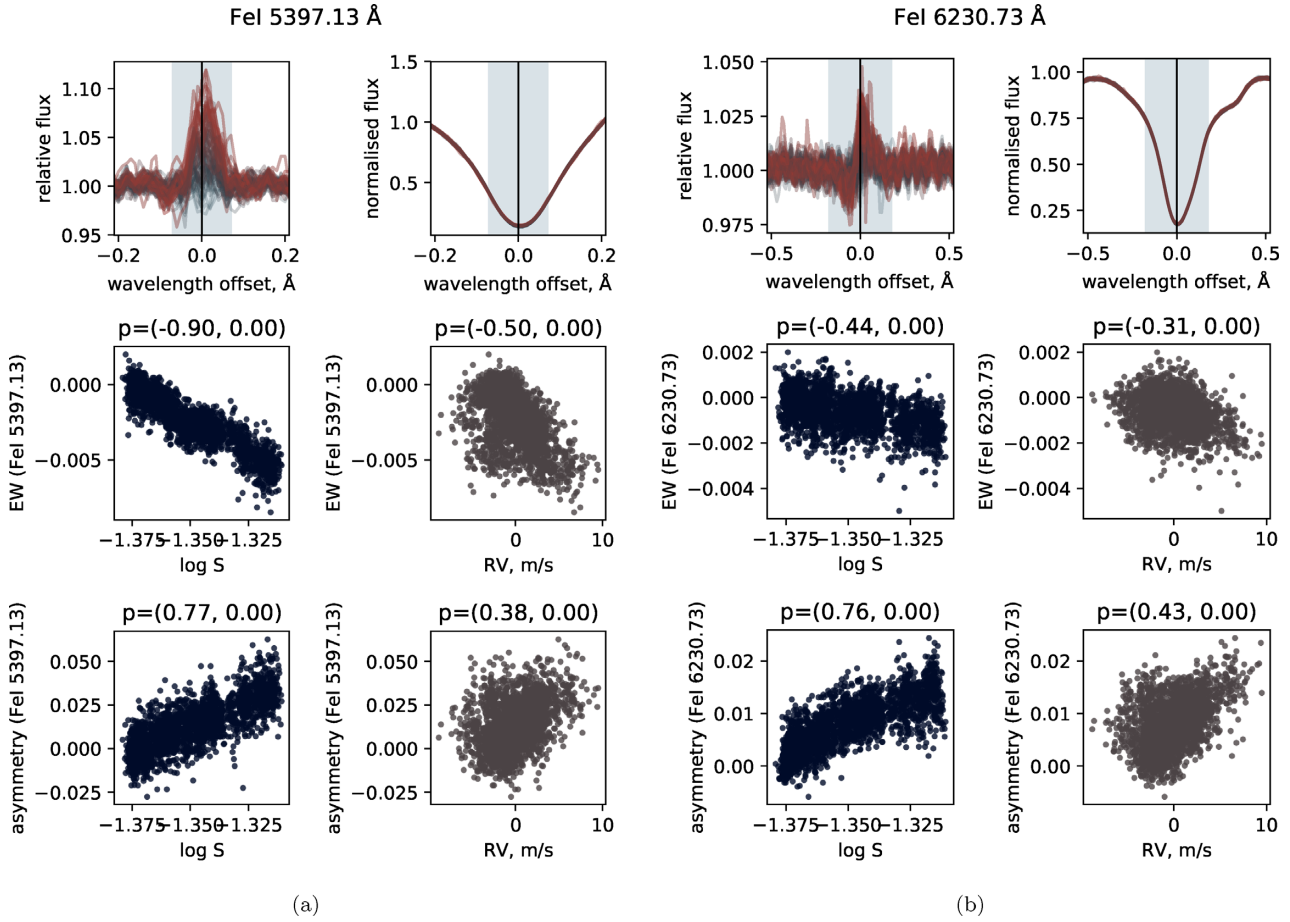

Figure 6. Two examples of the activity-sensitive lines, substantially changing in (a) flux and (b) shape. The plots show the relative spectrum (upper left, red indicates high activity spectrum, black–low activity), normalized spectrum (upper right, same colour scheme), log$S$ versus EW of the line (middle left), log$S$ versus asymmetry of the line (bottom left), RV versus EW of the line (middle right), and RV versus asymmetry of the line (bottom right).

The resulting general shape is well approximated with a third-order polynomial, but due to an imperfect blaze correction some spectra show continuum variations. To correct for this, the spectra were median binned by 10 Å and intepolated using cubic splines to identify the pseudo-continuum. The resulting relative spectra were overplotted and coloured based on S-index value for easy identification of active lines. We visually inspected the whole HARPS spectrum range for different line shape variations. A line was added to the list if its relative flux variation was above 2 per cent (the relative spectra have about 1 per cent noise level). The species were determined by comparing to the spectral atlas SPECTROWEB.

EWs of the lines (and their variations) were measured and asymmetries of the lines were quantified by subtracting mean flux in the right and left wings of the line. EWs were measured the same way as in the previous section (see equation 1). The line core was selected manually to contain all the flux variations, and the pseudo-continua were chosen to be non-varying parts of the spectra. Right and left wings here are parts of a line on either side of a measured centre with the same width (half width of the line core window).

In addition, we computed Pearson's correlation coefficients for both measured values compared to log$S$. The code used in this work to measure line variations is available on GITHUB.[2]

[2]https://github.com/timberhill/slice

4.2 Results

The full list of 345 activity-sensitive lines are given in Appendix A. These include the 40 lines compiled by Wise et al. (2018) and maybe comparable to the 489 lines found by Dumusque (2018). Visual inspection of the relative spectra produced much better results in the blue part of the spectrum which is less hampered by tellurics despite the higher noise and relative lack of continuum to rely on.

Ca H&K lines were used as a test case for correlation and an estimate of measurement discrepancy between Mount–Wilson S-index and EW from a relative spectrum. The correlation here has very small scatter and correlation coefficient close to 1, which is expected. Most lines correlate with S-index in either flux or asymmetry. Some are definitely sensitive to activity, but do not correlate with Ca H&K lines, which could mean the variations are produced via different processes. In addition, several spectral lines identified in Wise et al. (2018, e.g. Fe I 4602.95Å) do not show correlation between the EW and S-index. This is most likely because correlations in Wise et al. (2018) are obtained between S-index and core depth, central width, and RV, which measure different line properties that vary independently from each other.

All the lines listed vary in time in different ways – core flux, position, or shape. Inspecting the relative spectra reveals much more information than just the EW of a line. Fig. 6 shows two examples of lines changing in flux and in shape:

Downloaded from https://academic.oup.com/mnras/article-abstract/485/4/4804/5420427 by University of Hertfordshire user on 16 May 2019

(i) Fe I 5397.13Å line (Fig. 6a) changes substantially with activity and seems rather symmetrical.

(ii) Fe I 6230.73Å line (Fig. 6b) varies much less in total flux (only about 3 per cent), but rather in the difference of a mean flux in the red and blue wings.

All lines were compared to the RV measurements from HARPS DRS, but none show a strong correlation, apparently different lines are affected by the activity in different ways and therefore produce different RV shifts. RV measured from separate lines would show a strong correlation with line variations (Dumusque 2018). Even neighbouring lines like Fe I 5225.53 and Fe I 5227.19 show correlation and anticorrelation in flux, respectively. The same is happening to Cr I 4616.13 and Cr I 4621.93 in both flux and asymmetry variations.

Another type of features is blended lines, of which there are at least 25 in the list. Two species were specified for one line if two strong lines blended and the resulting feature had only one peak. If the two lines change in flux in a different way, the resulting blended feature will change shape and mock RV shifts. We suspect that a substantial amount of variations are caused by blending of strong lines with weaker features that also vary, but are not measurable in a reliable way, even with these high-S/N data.

5 DISCUSSION

We analysed HARPS observations of α Cen B and assessed the quality of the data. A number of observations were rejected due to bad quality spectra using independent proxies, providing a cleaner data set.

Telluric contamination was estimated using a pair of water lines in the spectrum. Those lines proved to be relatively good indicators as they do not blend with strong atomic features in the stellar spectrum over the course of a year. We put a limit on contamination using RV measurements of separate orders and identify those that are most affected. Only a small fraction of observations was too affected to be used. Removing the affected orders from RV measurements reduced disagreement between orders from about 4 to 2 m s^{-1}.

Activity in FGK stars is commonly estimated from only two Ca H&K lines. In this work, we present 345 spectral lines sensitive to activity. The number is much higher than in previous works for a variety of reasons including our focus on high resolution, high S/N spectra of a single star. We have visually inspected the selected lines to ensure robust identification of weaker lines and a variety of line shapes.

The line list includes lines throughout the spectral range considered including multiple lines in most spectral orders. Visual inspection of the relative spectra enables identification of a wide variety of different shape variations of the spectral lines that ultimately affect the RV measurements. Not all lines in the list correlate with Ca H&K lines, as measured by the EW variations and asymmetry, but all change in flux or shape (as expected due to the method used). As the lines originate in different pressure and temperature environments, they vary in different ways that affect RV measurements differently – core flux, wings, width, asymmetries, blended lines, etc. Even neighbouring spectral lines are affected differently, so measuring RV from individual lines (Dumusque 2018) of small wavelength ranges (Butler et al. 1996) will produce much better results. The list in Appendix A samples the whole HARPS spectral range and can be treated as a list of the most sensitive lines.

ACKNOWLEDGEMENTS

Based on observations collected at the European Organisation for Astronomical Research in the Southern Hemisphere under ESO programmes 076.C-0878(B), 074.C-0012(B), 072.C-0513(D), 082.C-0315(A), 183.C-0972(A), 083.C-1001(A), 084.C-0229(A), 085.C-0318(A), 088.C-0011(A), 091.C-0844(A), 086.C-0230(A), 087.C-0990(A), and 089.C-0050(A).

This research made use of NUMPY (Van Der Walt, Colbert & Varoquaux 2011), ASTROPY, a community-developed core PYTHON package for Astronomy (Astropy Collaboration 2013), SCIPY (Jones et al. 2001), SCIKIT-LEARN (McKinney 2010), and MATPLOTLIB, a PYTHON library for publication quality graphics (Hunter 2007). Spectral features were identified using SPECTROWEB,[3] interactive digital spectral atlases of bright stars (Lobel 2006, 2008, 2011).

ML is supported by a University of Hertfordshire PhD studentship. HJ and FF acknowledge support from the UK Science and Technology Facilities Council [ST/M001008/1].

REFERENCES

Anglada-Escudé G., Butler R. P., 2012, ApJS, 200, 15
Artigau É. et al., 2014, Proc. SPIE, 9149, 914905
Astropy Collaboration, 2013, A&A, 558, A33
Berdiñas Z. M., Amado P. J., Anglada-Escudé G., Rodríguez-López C., Barnes J., 2016, MNRAS, 459, 3551
Berdiñas Z. M., Rodríguez-López C., Amado P. J., Anglada-Escudé G., Barnes J. R., MacDonald J., Zechmeister M., Sarmiento L. F., 2017, MNRAS, 469, 4268
Bergmann C., Endl M., Hearnshaw J. B., Wittenmyer R. A., Wright D. J., 2015, Int. J. Astrobiol., 14, 173
Boisse I., Bouchy F., Hébrard G., Bonfils X., Santos N., Vauclair S., 2011, in Prasad Choudhary D., Strassmeier K. G., eds, IAU Symp. Vol. 273, Physics of Sun and Star Spots. Kluwer, Dordrecht, p. 281
Butler R. P., Marcy G. W., Williams E., McCarthy C., Dosanjh P., Vogt S. S., 1996, PASP, 108, 500
Cunha D., Santos N. C., Figueira P., Santerne A., Bertaux J. L., Lovis C., 2014, A&A, 568, A35
Davis A. B., Cisewski J., Dumusque X., Fischer D. A., Ford E. B., 2017, ApJ, 846, 59
Dumusque X. et al., 2012, Nature, 491, 207
Dumusque X., 2018, A&A, 620, A47
Duncan D. K. et al., 1991, ApJ, 76, 383
Feng F., Tuomi M., Jones H. R. A., Barnes J., Anglada-Escudé G., Vogt S. S., Butler R. P., 2017, AJ, 154, 135
Gomes da Silva J., Santos N. C., Bonfils X., Delfosse X., Forveille T., Udry S., 2011, A&A, 534, A30
Hatzes A. P., 2013, ApJ, 770, 133
Henry G. W., Newsom M. S., 1996, PASP, 108, 242
Huélamo N. et al., 2008, A&A, 489, L9
Hunter J. D., 2007, Comput. Sci. Eng., 9, 90
Hussain M., 1984, Sol. Energy, 33, 217
Jones E., et al., 2001, SciPy: Open Source Scientific Tools for Python. Available at: http://www.scipy.org/(Last accessed December 2018)
Kürster M. et al., 2003, A&A, 403, 1077
Lindegren L., Dravins D., 2003, A&A, 401, 1185
Lobel A., 2007, in Gomez de Castro A., Barstow M., eds, *Proc. XXVIth IAU Joint Discussion 4, The Ultraviolet Universe: Stars from Birth to Death*. Complutense Univ. Madrid Publ., Madrid, p. 167
Lobel A., 2008, J. Phys. Conf. Ser., 130, 012015
Lobel A., 2011, Can. J. Phys., 89, 395
Mayor M. et al., 2003, The Messenger, 114, 20
Mayor M., Queloz D., 1995, Nature, 378, 355

[3] http://spectra.freeshell.org

Downloaded from https://academic.oup.com/mnras/article-abstract/485/4/4804/5420427 by University of Hertfordshire user on 16 May 2019

McKinney W., 2010, in van der Walt S., Millman J., eds, Proc. 9th Python in Science Conference, *Data Structures for Statistical Computing in Python*, p. 51
O'Toole S. J., Tinney C. G., Jones H. R. A., 2008, MNRAS, 386, 516
Queloz D. et al., 2001, A&A, 379, 279
Rajpaul V., Aigrain S., Roberts S., 2016, MNRAS, 456, L6
Saar S. H., Donahue R. A., 1997, ApJ, 485, 319
Santos N. C., Mayor M., Naef D., Queloz D., Udry S., 2001, in Penny A., Artymowicz P., Lagrange A.-M., Russell S., eds, Proc. XXIV IAU General Assembly, IAU Symposium S202 "Planetary Systems in the Universe", preprint (arXiv:astro-ph/0101377v1)
Santos N. C., Gomes da Silva J., Lovis C., Melo C., 2010, A&A, 511, A54
Struve O., 1952, The Observatory, 72, 199
Thompson A. P. G., Watson C. A., de Mooij E. J. W., Jess D. B., 2017, MNRAS, 468, L16
Van Der Walt S., Colbert S. C., Varoquaux G., 2011, Comput. Sci. Eng., 13, 22
Wilson O. C., 1978, ApJ, 226, 379
Wise A. W., Dodson-Robinson S. E., Bevenour K., Provini A., 2018, AJ, 156, 180
Wolszczan A., Frail D. A., 1992, Nature, 355, 145
Wright D. J., Wittenmyer R. A., Tinney C. G., Bentley J. S., Zhao J., 2016, ApJ, 817, L20
Zhao L., Fischer D. A., Brewer J., Giguere M., Rojas-Ayala B., 2018, AJ, 155, 24

SUPPORTING INFORMATION

Supplementary data are available at *MNRAS* online.

aCenB_HARPS_clean.dat The final list of observations used, including filenames, CCF and line measurements.
appendix.dat A list of activity sensitive spectral lines and and measurements, as in the Appendix.
Please note: Oxford University Press is not responsible for the content or functionality of any supporting materials supplied by the authors. Any queries (other than missing material) should be directed to the corresponding author for the article.

APPENDIX A: ACTIVITY-SENSITIVE LINES IDENTIFIED IN THIS WORK

Table A1. The activity-sensitive lines presented below are also available as a supplementary online table. The table includes measured centre, species, equivalent width of the line (EW, measured from a low activity template), change in equivalent width (ΔEW, measured from relative spectra), Pearson's correlation coefficient and two-tailed *p*-value for log*S* versus ΔEW (ΔEW PCC), Asymmetry of the line – difference between mean flux in the red and blue wings. Pearson's correlation coefficient and two-tailed *p*-value for log*S* versus Asymmetry (Asym. PCC).

Centre	Species	EW	ΔEW[1]	ΔEW PCC[2]	Asym.[3]	Asym. PCC[4]
3824.45	Fe I	0.1170	− 0.0202	(− 0.38, 0.00)	0.0132	(0.12, 0.00)
3849.01	La II	0.0931	− 0.0177	(− 0.51, 0.00)	0.0066	(0.12, 0.00)
3856.38	Fe I	0.1264	− 0.0150	(− 0.28, 0.00)	− 0.0478	(0.07, 0.00)
3859.92	Fe I	0.1689	− 0.0253	(− 0.46, 0.00)	0.0026	(0.07, 0.00)
3878.02	Fe I	0.1123	− 0.0151	(− 0.35, 0.00)	0.0018	(0.21, 0.00)
3878.58	Fe I	0.1122	− 0.0313	(− 0.61, 0.00)	0.1114	(0.44, 0.00)
3886.28	Fe I	0.1381	− 0.0118	(− 0.38, 0.00)	0.0409	(0.18, 0.00)
3895.66	Fe I	0.1034	− 0.0088	(− 0.38, 0.00)	0.0736	(0.21, 0.00)
3899.71	Fe I	0.0655	− 0.0079	(− 0.44, 0.00)	0.0301	(0.15, 0.00)
3905.53	Si I	0.1317	− 0.0079	(− 0.40, 0.00)	0.0154	(0.07, 0.00)
3907.94	Fe I	0.0614	− 0.0049	(− 0.33, 0.00)	0.0219	(0.20, 0.00)
3908.76	Cr I	0.0957	0.0052	(0.31, 0.00)	0.0035	(0.10, 0.00)
3914.33	Ti I + V II	0.1408	− 0.0012	(− 0.24, 0.00)	− 0.0008	(0.20, 0.00)
3917.19	Fe I	0.1379	− 0.0039	(− 0.33, 0.00)	0.0155	(− 0.01, 0.64)
3920.26	Fe I	0.0658	− 0.0030	(− 0.48, 0.00)	0.0157	(0.23, 0.00)
3922.92	Fe I	0.1227	− 0.0108	(− 0.67, 0.00)	0.0065	(0.19, 0.00)
3927.93	Fe I	0.1218	− 0.0124	(− 0.50, 0.00)	0.0216	(0.29, 0.00)
3930.30	Fe I	0.1294	− 0.0126	(− 0.55, 0.00)	0.0254	(0.20, 0.00)
3933.68	Ca K	0.4170	− 0.3205	(− 0.97, 0.00)	− 0.0113	(− 0.18, 0.00)
3944.01	Al I	0.9292	− 0.0255	(− 0.67, 0.00)	0.0010	(0.21, 0.00)
3961.53	Al I	0.9980	− 0.0391	(− 0.63, 0.00)	0.0023	(0.00, 0.92)
3968.47	Ca H	0.3971	− 0.2592	(− 0.97, 0.00)	0.0323	(0.64, 0.00)
4020.90	Co I	0.1019	− 0.0024	(− 0.33, 0.00)	0.0021	(0.15, 0.00)
4032.63	Fe I	0.0611	− 0.0028	(− 0.34, 0.00)	0.0254	(0.39, 0.00)
4045.82	Fe I	1.5571	− 0.0300	(− 0.79, 0.00)	0.0026	(0.25, 0.00)
4048.75	Mn I	0.1018	− 0.0015	(− 0.21, 0.00)	0.0120	(0.14, 0.00)
4055.55	Mn I	0.0874	− 0.0036	(− 0.47, 0.00)	0.0093	(0.21, 0.00)
4058.93	Mn I + Ca I	0.0688	− 0.0011	(− 0.34, 0.00)	0.0168	(0.12, 0.00)
4061.73	Mn I	0.0937	− 0.0028	(− 0.59, 0.00)	− 0.0058	(− 0.07, 0.00)
4063.60	Fe I	1.2458	− 0.0350	(− 0.78, 0.00)	0.0033	(0.08, 0.00)
4071.74	Fe I	1.1328	− 0.0190	(− 0.80, 0.00)	− 0.0006	(0.14, 0.00)
4077.72	Sr II	0.1102	− 0.0014	(− 0.04, 0.08)	0.0145	(0.21, 0.00)
4092.68	V I	0.1091	− 0.0025	(− 0.60, 0.00)	− 0.0226	(− 0.08, 0.00)
4099.79	V I	0.0772	− 0.0014	(− 0.43, 0.00)	0.0121	(0.28, 0.00)
4100.74	Fe I	0.0702	− 0.0006	(− 0.20, 0.00)	0.0283	(0.40, 0.00)

Downloaded from https://academic.oup.com/mnras/article-abstract/485/4/4804/5420427 by University of Hertfordshire user on 16 May 2019

Table A1 – *continued*

Centre	Species	EW	ΔEW[1]	ΔEW PCC[2]	Asym.[3]	Asym. PCC[4]
4102.94	Si I	0.0765	−0.0022	(−0.63, 0.00)	0.0126	(0.30, 0.00)
4109.80	Fe I + V I	0.1047	−0.0018	(−0.53, 0.00)	−0.0106	(−0.24, 0.00)
4110.54	Co I	0.0949	−0.0021	(−0.57, 0.00)	−0.0009	(0.08, 0.00)
4111.78	V I	0.0786	−0.0022	(−0.63, 0.00)	0.0047	(0.24, 0.00)
4115.18	V I	0.0837	−0.0019	(−0.53, 0.00)	0.0153	(0.26, 0.00)
4116.48	V I	0.0573	−0.0019	(−0.67, 0.00)	0.0141	(0.27, 0.00)
4116.55	V I	0.0566	−0.0022	(−0.79, 0.00)	0.0037	(−0.26, 0.00)
4121.32	Co I	0.0891	−0.0032	(−0.40, 0.00)	0.0300	(0.38, 0.00)
4121.81	Fe I	0.0936	0.0025	(0.63, 0.00)	−0.0018	(−0.12, 0.00)
4132.06	Fe I	0.3144	−0.0072	(−0.73, 0.00)	0.0015	(−0.06, 0.01)
4143.87	Fe I	0.0908	−0.0031	(−0.32, 0.00)	0.0248	(0.34, 0.00)
4147.67	Fe I	0.0619	−0.0026	(−0.36, 0.00)	0.0352	(0.41, 0.00)
4174.92	Fe I	0.0782	−0.0035	(−0.55, 0.00)	−0.0069	(−0.13, 0.00)
4177.60	Fe I	0.0646	−0.0015	(−0.44, 0.00)	0.0070	(0.03, 0.14)
4180.83	V II	0.1390	−0.0048	(−0.80, 0.00)	0.0088	(0.40, 0.00)
4187.04	Fe I	0.0803	−0.0002	(0.06, 0.01)	0.0256	(0.38, 0.00)
4190.71	Co I	0.1093	−0.0034	(−0.81, 0.00)	0.0096	(0.38, 0.00)
4206.70	Fe I	0.0628	−0.0038	(−0.77, 0.00)	0.0198	(0.20, 0.00)
4216.19	Fe I	0.0715	−0.0062	(−0.87, 0.00)	0.0186	(0.34, 0.00)
4226.73	Ca I	2.0420	−0.0550	(−0.93, 0.00)	0.0024	(0.21, 0.00)
4246.83	Sc II	0.0713	−0.0009	(−0.03, 0.23)	0.0147	(0.49, 0.00)
4250.12	Fe I	0.0764	0.0002	(−0.03, 0.16)	0.0422	(0.40, 0.00)
4250.79	Fe I	0.0870	−0.0018	(−0.35, 0.00)	0.0360	(0.42, 0.00)
4252.30	Co I	0.0744	−0.0031	(−0.80, 0.00)	0.0101	(0.23, 0.00)
4254.34	Cr I	0.5104	−0.0225	(−0.80, 0.00)	0.0127	(0.37, 0.00)
4258.32	Fe I	0.0731	−0.0016	(−0.36, 0.00)	0.0192	(0.42, 0.00)
4281.37	Ti I	0.0426	−0.0011	(−0.58, 0.00)	−0.0190	(−0.20, 0.00)
4291.47	Fe I	0.0680	−0.0021	(−0.65, 0.00)	0.0235	(0.43, 0.00)
4294.13	Fe I + Ti II	0.1175	−0.0040	(−0.69, 0.00)	−0.0007	(0.02, 0.35)
4298.99	Ca I	0.0488	−0.0013	(−0.13, 0.00)	0.0419	(0.34, 0.00)
4318.65	Ca I	0.0818	−0.0007	(−0.05, 0.01)	0.0155	(0.44, 0.00)
4320.74	Sc II	0.1094	0.0019	(0.66, 0.00)	0.0053	(0.18, 0.00)
4325.77	Fe I	0.1348	−0.0034	(−0.20, 0.00)	0.0059	(0.19, 0.00)
4330.02	V I	0.0710	−0.0018	(−0.74, 0.00)	0.0016	(0.19, 0.00)
4337.05	Fe I	0.0803	−0.0011	(−0.38, 0.00)	0.0256	(0.49, 0.00)
4337.92	Ti II	0.0860	0.0026	(0.66, 0.00)	0.0024	(0.12, 0.00)
4340.49	Hγ	0.3110	0.0222	(0.94, 0.00)	−0.0007	(0.22, 0.00)
4341.00	V I	0.0587	−0.0014	(−0.67, 0.00)	0.0133	(0.43, 0.00)
4351.77	Fe II	0.1050	−0.0032	(−0.67, 0.00)	0.0199	(0.42, 0.00)
4351.91	Mg I	0.1116	−0.0011	(−0.32, 0.00)	0.0198	(0.31, 0.00)
4352.74	Fe I	0.0854	−0.0001	(0.19, 0.00)	0.0031	(0.45, 0.00)
4352.87	V I	0.1184	−0.0019	(−0.70, 0.00)	0.0182	(0.54, 0.00)
4367.91	Fe I	0.0601	−0.0001	(0.20, 0.00)	0.0126	(0.29, 0.00)
4368.05	V I	0.0365	−0.0011	(−0.50, 0.00)	−0.0024	(0.13, 0.00)
4371.28	Cr I	0.0861	0.0003	(0.30, 0.00)	0.0178	(0.34, 0.00)
4374.16	Cr I	0.0995	−0.0017	(−0.60, 0.00)	0.0097	(0.51, 0.00)
4374.47	Sc II	0.0581	−0.0003	(−0.08, 0.00)	0.0122	(0.13, 0.00)
4375.94	Fe I	0.0693	−0.0098	(−0.95, 0.00)	0.0364	(0.42, 0.00)
4379.23	V I	0.1136	−0.0040	(−0.74, 0.00)	0.0188	(0.41, 0.00)
4383.55	Fe I	1.8531	−0.0406	(−0.89, 0.00)	0.0017	(0.31, 0.00)
4389.25	Fe I	0.0636	−0.0001	(−0.26, 0.00)	0.0384	(0.54, 0.00)
4389.99	V I	0.1018	−0.0014	(−0.35, 0.00)	0.0126	(0.17, 0.00)
4395.04	Ti II	0.1283	0.0025	(0.78, 0.00)	0.0083	(−0.01, 0.52)
4395.23	V I	0.0838	−0.0008	(−0.60, 0.00)	0.0303	(0.60, 0.00)
4399.77	Ti II	0.1057	0.0019	(0.54, 0.00)	−0.0032	(0.13, 0.00)
4404.76	Fe I	1.1583	−0.0252	(−0.90, 0.00)	−0.0007	(−0.07, 0.00)
4406.64	V I	0.0970	−0.0022	(−0.81, 0.00)	0.0115	(0.38, 0.00)
4407.68	Fe I	0.1438	−0.0038	(−0.76, 0.00)	−0.0185	(−0.48, 0.00)
4408.20	V I	0.0932	−0.0006	(−0.41, 0.00)	0.0096	(0.40, 0.00)
4408.47	Fe I	0.1700	−0.0040	(−0.67, 0.00)	0.0053	(0.37, 0.00)
4416.47	V I	0.0816	−0.0018	(−0.64, 0.00)	−0.0007	(0.44, 0.00)
4421.57	V I	0.0480	−0.0016	(−0.66, 0.00)	0.0171	(0.42, 0.00)

Downloaded from https://academic.oup.com/mnras/article-abstract/485/4/4804/5420427 by University of Hertfordshire user on 16 May 2019

Table A1 – *continued*

Centre	Species	EW	ΔEW[1]	ΔEW PCC[2]	Asym.[3]	Asym. PCC[4]
4426.02	V I + Ti I	0.0861	− 0.0035	(− 0.76, 0.00)	− 0.0057	(− 0.24, 0.00)
4427.32	Fe I	0.0942	− 0.0093	(− 0.94, 0.00)	0.0200	(0.37, 0.00)
4428.52	V I + Cr I	0.0883	− 0.0019	(− 0.70, 0.00)	0.0090	(0.34, 0.00)
4429.79	V I	0.0775	− 0.0016	(− 0.77, 0.00)	0.0022	(0.36, 0.00)
4435.15	Fe I	0.0773	− 0.0011	(− 0.58, 0.00)	0.0176	(0.57, 0.00)
4436.14	V I	0.0581	− 0.0015	(− 0.76, 0.00)	− 0.0001	(0.19, 0.00)
4437.83	V I	0.0780	− 0.0021	(− 0.67, 0.00)	0.0066	(0.53, 0.00)
4439.88	Fe I	0.0668	0.0018	(0.52, 0.00)	0.0023	(0.16, 0.00)
4441.69	Ti II + V I	0.0876	− 0.0019	(− 0.77, 0.00)	0.0060	(0.31, 0.00)
4442.34	Fe I	0.0883	− 0.0007	(− 0.38, 0.00)	0.0287	(0.54, 0.00)
4443.81	Ti II	0.0817	0.0001	(0.43, 0.00)	0.0083	(0.18, 0.00)
4444.21	V I	0.0854	− 0.0015	(− 0.72, 0.00)	0.0174	(0.61, 0.00)
4451.59	Mn I	0.1196	− 0.0005	(0.33, 0.00)	0.0030	(0.18, 0.00)
4452.01	V I	0.0775	− 0.0014	(− 0.60, 0.00)	0.0014	(0.02, 0.39)
4454.39	Fe I	0.1336	0.0008	(0.53, 0.00)	0.0013	(0.15, 0.00)
4455.32	Ti I + Mn I	0.1220	− 0.0014	(− 0.06, 0.00)	0.0035	(0.03, 0.10)
4455.89	Ca I	0.0712	− 0.0012	(− 0.41, 0.00)	0.0301	(0.23, 0.00)
4457.50	Mn I + V I	0.1576	− 0.0030	(− 0.73, 0.00)	− 0.0065	(− 0.22, 0.00)
4459.76	V I	0.0972	− 0.0024	(− 0.71, 0.00)	− 0.0019	(0.08, 0.00)
4460.30	V I	0.1294	− 0.0044	(− 0.83, 0.00)	0.0170	(0.36, 0.00)
4461.66	Fe I	0.1144	− 0.0078	(− 0.93, 0.00)	0.0171	(0.64, 0.00)
4466.57	Fe I	0.1262	− 0.0020	(− 0.61, 0.00)	0.0270	(0.51, 0.00)
4468.50	Ti II	0.1221	0.0028	(0.80, 0.00)	− 0.0015	(0.03, 0.15)
4472.76	Fe I	0.1345	− 0.0018	(− 0.71, 0.00)	0.0016	(0.37, 0.00)
4482.18	Fe I	0.1371	− 0.0085	(− 0.93, 0.00)	0.0688	(0.84, 0.00)
4482.73	Fe I	0.1038	− 0.0007	(− 0.43, 0.00)	− 0.0083	(− 0.45, 0.00)
4489.74	Fe I	0.1263	− 0.0008	(− 0.46, 0.00)	0.0170	(0.70, 0.00)
4494.57	Fe I	0.1555	− 0.0004	(− 0.32, 0.00)	0.0019	(0.30, 0.00)
4496.86	Cr I	0.1475	0.0014	(0.56, 0.00)	0.0054	(0.20, 0.00)
4501.27	Ti II	0.1159	0.0020	(0.74, 0.00)	0.0068	(0.20, 0.00)
4512.74	Ti I	0.0959	0.0002	(0.41, 0.00)	0.0045	(0.22, 0.00)
4514.47	Cr I	0.1266	− 0.0011	(− 0.62, 0.00)	0.0004	(− 0.21, 0.00)
4518.03	Ti I	0.1087	0.0010	(0.53, 0.00)	− 0.0018	(0.02, 0.33)
4522.80	Ti I	0.1057	0.0009	(0.53, 0.00)	0.0056	(0.40, 0.00)
4528.62	Fe I	0.3556	− 0.0035	(− 0.73, 0.00)	0.0008	(0.32, 0.00)
4531.15	Fe I	0.1437	− 0.0004	(− 0.37, 0.00)	0.0249	(0.64, 0.00)
4533.25	Ti I	0.1473	0.0012	(0.33, 0.00)	0.0051	(0.20, 0.00)
4533.97	Ti II	0.1237	0.0024	(0.79, 0.00)	0.0082	(0.18, 0.00)
4534.78	Ti I	0.1383	0.0014	(0.43, 0.00)	0.0096	(0.39, 0.00)
4544.68	Ti I	0.1524	− 0.0004	(− 0.20, 0.00)	− 0.0071	(− 0.32, 0.00)
4545.35	Cr I	0.0879	− 0.0020	(− 0.66, 0.00)	0.0072	(0.53, 0.00)
4545.96	Cr I	0.1233	0.0013	(0.67, 0.00)	0.0017	(0.23, 0.00)
4549.63	Ti II	0.2352	0.0032	(0.79, 0.00)	0.0047	(0.42, 0.00)
4554.03	Ba II	0.1755	0.0029	(0.70, 0.00)	− 0.0010	(− 0.00, 0.92)
4563.76	Ti II	0.1288	0.0026	(0.75, 0.00)	− 0.0047	(− 0.09, 0.00)
4571.10	Mg I	0.1023	− 0.0046	(− 0.91, 0.00)	0.0130	(0.48, 0.00)
4571.98	Ti II	0.1412	0.0042	(0.85, 0.00)	− 0.0014	(− 0.09, 0.00)
4577.18	V I	0.0753	− 0.0013	(− 0.65, 0.00)	− 0.0019	(0.14, 0.00)
4586.37	V I	0.1008	− 0.0017	(− 0.67, 0.00)	0.0090	(0.33, 0.00)
4592.66	Fe I	0.1295	0.0006	(0.29, 0.00)	0.0069	(0.19, 0.00)
4594.12	V I	0.1070	− 0.0024	(− 0.74, 0.00)	0.0084	(0.37, 0.00)
4600.75	Cr I	0.1144	0.0016	(0.53, 0.00)	0.0081	(0.42, 0.00)
4602.95	Fe I	0.1641	− 0.0003	(0.01, 0.61)	0.0044	(0.32, 0.00)
4616.13	Cr I	0.1174	0.0026	(0.80, 0.00)	0.0057	(0.16, 0.00)
4621.93	Cr I	0.0885	− 0.0012	(− 0.70, 0.00)	− 0.0005	(− 0.32, 0.00)
4626.18	Cr I	0.1193	0.0034	(0.77, 0.00)	0.0048	(0.23, 0.00)
4629.35	Fe II	0.1070	− 0.0010	(− 0.24, 0.00)	0.0052	(0.36, 0.00)
4632.91	Fe I	0.0648	− 0.0006	(− 0.19, 0.00)	0.0303	(0.44, 0.00)
4645.19	Ti I	0.0542	− 0.0008	(− 0.41, 0.00)	0.0033	(0.29, 0.00)
4646.17	Cr I	0.1376	0.0031	(0.70, 0.00)	0.0039	(0.17, 0.00)
4647.44	Fe I	0.1017	0.0009	(0.58, 0.00)	0.0014	(0.27, 0.00)
4651.29	Cr I	0.1109	0.0019	(0.75, 0.00)	0.0084	(0.44, 0.00)
4652.16	Cr I	0.1411	0.0013	(0.57, 0.00)	0.0081	(0.55, 0.00)
4656.47	Ti I	0.0965	− 0.0002	(0.25, 0.00)	0.0056	(0.41, 0.00)

Downloaded from https://academic.oup.com/mnras/article-abstract/485/4/4804/5420427 by University of Hertfordshire user on 16 May 2019

Table A1 *– continued*

Centre	Species	EW	ΔEW[1]	ΔEW PCC[2]	Asym.[3]	Asym. PCC[4]
4675.11	Fe I + Ti I	0.0668	−0.0013	(−0.56, 0.00)	0.0044	(0.37, 0.00)
4681.91	Ti I	0.0999	0.0003	(0.19, 0.00)	0.0109	(0.57, 0.00)
4715.30	Ti I	0.0382	−0.0008	(−0.66, 0.00)	0.0096	(0.28, 0.00)
4722.16	Zn I	0.0763	0.0002	(0.16, 0.00)	−0.0103	(−0.32, 0.00)
4722.61	Ti I	0.0513	−0.0010	(−0.47, 0.00)	0.0028	(0.16, 0.00)
4723.16	Ti I	0.0915	−0.0018	(−0.70, 0.00)	−0.0017	(−0.15, 0.00)
4733.60	Fe I	0.1151	0.0014	(0.59, 0.00)	0.0042	(0.09, 0.00)
4736.78	Fe I	0.1301	0.0005	(0.22, 0.00)	0.0019	(0.31, 0.00)
4754.04	Mn I	0.1578	−0.0007	(−0.22, 0.00)	0.0083	(0.40, 0.00)
4759.27	Ti I	0.0704	−0.0002	(−0.12, 0.00)	0.0056	(0.20, 0.00)
4761.53	Mn I	0.0860	−0.0006	(−0.08, 0.00)	0.0046	(−0.05, 0.01)
4762.38	Mn I	0.1255	−0.0000	(−0.02, 0.45)	0.0099	(0.26, 0.00)
4772.82	Fe I	0.1156	0.0004	(0.13, 0.00)	0.0062	(0.50, 0.00)
4783.42	Mn I	0.2302	−0.0005	(−0.15, 0.00)	0.0039	(0.33, 0.00)
4823.51	Mn I	0.1629	0.0004	(0.06, 0.00)	0.0117	(0.37, 0.00)
4827.46	V I	0.0739	−0.0025	(−0.89, 0.00)	0.0039	(0.09, 0.00)
4831.65	V I	0.0713	−0.0020	(−0.79, 0.00)	0.0085	(0.42, 0.00)
4832.43	V I	0.0607	−0.0016	(−0.66, 0.00)	0.0065	(0.22, 0.00)
4840.88	Ti I + Fe I	0.0952	0.0006	(0.41, 0.00)	0.0019	(0.22, 0.00)
4851.50	V I	0.0784	−0.0024	(−0.81, 0.00)	0.0060	(0.20, 0.00)
4859.75	Fe I	0.1710	0.0024	(0.63, 0.00)	0.0061	(0.21, 0.00)
4861.33	Hβ	0.5264	0.0286	(0.94, 0.00)	−0.0062	(−0.68, 0.00)
4875.49	V I	0.0897	−0.0019	(−0.73, 0.00)	−0.0002	(0.19, 0.00)
4881.56	V I	0.1124	−0.0020	(−0.81, 0.00)	0.0098	(0.40, 0.00)
4890.76	Fe I	0.1111	0.0005	(0.27, 0.00)	0.0083	(0.33, 0.00)
4891.50	Fe I	0.0895	0.0002	(0.02, 0.39)	0.0213	(0.38, 0.00)
4920.51	Fe I	0.5394	−0.0043	(−0.63, 0.00)	0.0054	(0.43, 0.00)
4923.93	Fe II	0.1256	0.0029	(0.82, 0.00)	0.0045	(0.16, 0.00)
4934.08	Ba II	0.1514	−0.0001	(0.25, 0.00)	−0.0072	(−0.54, 0.00)
4938.82	Fe I	0.1426	0.0005	(0.55, 0.00)	0.0047	(0.41, 0.00)
4939.69	Fe I	0.1204	0.0001	(−0.12, 0.00)	0.0102	(0.60, 0.00)
4942.49	Cr I + Fe I	0.1204	−0.0015	(−0.37, 0.00)	0.0057	(0.37, 0.00)
4981.74	Ti I	0.1480	0.0014	(0.48, 0.00)	0.0012	(0.24, 0.00)
4991.07	Ti I	0.1501	−0.0002	(0.48, 0.00)	0.0114	(0.56, 0.00)
4994.13	Fe I	0.1072	−0.0006	(−0.54, 0.00)	0.0233	(0.75, 0.00)
4999.51	Ti I	0.1412	0.0005	(0.53, 0.00)	0.0041	(0.21, 0.00)
5007.22	Ti I + Fe I	0.1567	−0.0007	(−0.36, 0.00)	0.0210	(0.68, 0.00)
5009.65	Ti I	0.0625	−0.0009	(−0.57, 0.00)	0.0106	(0.51, 0.00)
5012.08	Fe I	0.1013	−0.0056	(−0.93, 0.00)	0.0202	(0.61, 0.00)
5013.30	Ti I + Cr I	0.0973	−0.0004	(−0.40, 0.00)	0.0055	(0.35, 0.00)
5014.23	Ti I + Ni I	0.1650	−0.0030	(−0.68, 0.00)	0.0081	(0.18, 0.00)
5016.17	Ti I	0.0759	−0.0002	(0.18, 0.00)	0.0085	(0.25, 0.00)
5018.44	Fe II	0.1515	0.0028	(0.88, 0.00)	−0.0003	(−0.09, 0.00)
5020.03	Ti I	0.0629	−0.0004	(−0.02, 0.28)	0.0198	(0.50, 0.00)
5022.87	Ti I	0.1026	0.0009	(0.50, 0.00)	0.0061	(0.31, 0.00)
5024.85	Ti I	0.1063	0.0004	(0.47, 0.00)	0.0033	(0.04, 0.04)
5039.96	Ti I	0.1119	0.0015	(0.55, 0.00)	0.0077	(0.33, 0.00)
5040.90	Fe I	0.0863	−0.0005	(−0.49, 0.00)	−0.0038	(−0.16, 0.00)
5041.08	Fe I	0.0975	−0.0016	(−0.68, 0.00)	0.0003	(0.24, 0.00)
5041.76	Fe I	0.0769	−0.0019	(−0.69, 0.00)	0.0252	(0.62, 0.00)
5051.64	Fe I	0.0649	−0.0040	(−0.88, 0.00)	0.0241	(0.63, 0.00)
5060.08	Fe I	0.0733	−0.0008	(−0.55, 0.00)	0.0093	(0.27, 0.00)
5064.66	Ti I	0.0841	−0.0005	(−0.32, 0.00)	0.0056	(0.30, 0.00)
5068.77	Fe I	0.1487	−0.0004	(0.14, 0.00)	0.0074	(0.24, 0.00)
5079.75	Fe I	0.1031	−0.0018	(−0.25, 0.00)	0.0117	(0.38, 0.00)
5083.34	Fe I	0.1419	−0.0006	(−0.10, 0.00)	0.0104	(0.54, 0.00)
5098.70	Fe I	0.0903	−0.0003	(−0.06, 0.00)	0.0133	(0.63, 0.00)
5105.54	Cu I	0.1205	−0.0007	(−0.28, 0.00)	0.0020	(0.08, 0.00)
5107.45	Fe I	0.1350	−0.0014	(−0.53, 0.00)	0.0102	(0.67, 0.00)
5107.65	Fe I	0.1289	0.0003	(0.43, 0.00)	−0.0034	(0.32, 0.00)
5110.41	Fe I	0.1019	−0.0080	(−0.96, 0.00)	0.0471	(0.84, 0.00)
5115.40	Ni I	0.0886	0.0005	(0.20, 0.00)	−0.0110	(−0.54, 0.00)
5123.73	Fe I	0.1333	−0.0010	(−0.45, 0.00)	0.0070	(0.49, 0.00)
5127.36	Fe I	0.1189	0.0001	(0.14, 0.00)	0.0155	(0.60, 0.00)

Downloaded from https://academic.oup.com/mnras/article-abstract/485/4/4804/5420427 by University of Hertfordshire user on 16 May 2019

Table A1 – *continued*

Centre	Species	EW	ΔEW[1]	ΔEW PCC[2]	Asym.[3]	Asym. PCC[4]
5142.93	Ni I	0.0962	− 0.0014	(− 0.72, 0.00)	0.0306	(0.74, 0.00)
5147.48	Ti I	0.0618	− 0.0010	(− 0.60, 0.00)	0.0182	(0.56, 0.00)
5150.85	Fe I	0.1391	− 0.0017	(− 0.61, 0.00)	0.0175	(0.72, 0.00)
5151.91	Fe I	0.1317	− 0.0004	(− 0.06, 0.00)	0.0012	(0.28, 0.00)
5152.19	Ti I	0.0669	− 0.0009	(− 0.47, 0.00)	0.0095	(0.52, 0.00)
5166.29	Fe I	0.0895	− 0.0042	(− 0.91, 0.00)	0.0177	(0.27, 0.00)
5167.33	Mg I	0.1383	− 0.0050	(− 0.87, 0.00)	0.0174	(0.47, 0.00)
5167.49	Fe I	0.1541	− 0.0036	(− 0.82, 0.00)	0.0165	(0.65, 0.00)
5168.90	Fe I	0.1353	− 0.0025	(− 0.82, 0.00)	0.0205	(0.81, 0.00)
5171.60	Fe I	0.1257	− 0.0025	(− 0.73, 0.00)	0.0288	(0.77, 0.00)
5172.69	Mg I	0.1713	− 0.0046	(− 0.77, 0.00)	0.0144	(0.42, 0.00)
5183.61	Mg I	2.2932	− 0.0430	(− 0.90, 0.00)	− 0.0023	(− 0.35, 0.00)
5191.46	Fe I	0.1522	0.0019	(0.67, 0.00)	0.0059	(0.43, 0.00)
5192.97	Ti I	0.0834	− 0.0005	(− 0.34, 0.00)	0.0243	(0.72, 0.00)
5194.95	Fe I	0.1405	− 0.0013	(− 0.49, 0.00)	0.0086	(0.60, 0.00)
5198.71	Fe I	0.1069	0.0002	(0.23, 0.00)	0.0129	(0.59, 0.00)
5202.34	Fe I	0.1853	− 0.0031	(− 0.51, 0.00)	− 0.0097	(− 0.22, 0.00)
5204.53	Cr I + Fe I	0.2380	− 0.0062	(− 0.87, 0.00)	0.0429	(0.91, 0.00)
5206.04	Cr I	0.3478	− 0.0013	(− 0.33, 0.00)	0.0073	(0.53, 0.00)
5208.43	Cr I	0.1327	0.0006	(0.22, 0.00)	0.0175	(0.50, 0.00)
5210.39	Ti I	0.0980	− 0.0007	(− 0.40, 0.00)	0.0221	(0.65, 0.00)
5216.28	Fe I	0.1129	− 0.0002	(− 0.27, 0.00)	0.0108	(0.46, 0.00)
5219.70	Ti I	0.0669	− 0.0005	(− 0.49, 0.00)	0.0003	(0.51, 0.00)
5225.53	Fe I	0.1026	0.0018	(0.77, 0.00)	0.0110	(0.60, 0.00)
5227.19	Fe I	0.1644	− 0.0046	(− 0.87, 0.00)	0.0132	(0.50, 0.00)
5238.58	Ti I	0.0590	− 0.0013	(− 0.76, 0.00)	0.0013	(0.08, 0.00)
5247.05	Fe I	0.0997	0.0010	(0.47, 0.00)	0.0066	(0.55, 0.00)
5247.57	Cr I	0.1271	0.0009	(0.53, 0.00)	0.0046	(0.50, 0.00)
5250.21	Fe I	0.0974	0.0007	(0.54, 0.00)	0.0084	(0.55, 0.00)
5254.96	Fe I	0.1180	− 0.0011	(− 0.51, 0.00)	0.0006	(− 0.03, 0.16)
5264.17	Cr I	0.1472	− 0.0023	(− 0.70, 0.00)	0.0297	(0.81, 0.00)
5269.54	Fe I	0.2483	− 0.0087	(− 0.94, 0.00)	0.0150	(0.67, 0.00)
5270.32	Fe I	0.2694	− 0.0068	(− 0.90, 0.00)	0.0039	(0.40, 0.00)
5298.28	Cr I	0.0969	− 0.0008	(− 0.32, 0.00)	0.0318	(0.60, 0.00)
5341.03	Fe I + Mn I	0.1799	− 0.0052	(− 0.78, 0.00)	0.0263	(0.49, 0.00)
5345.80	Cr I	0.1107	− 0.0006	(− 0.05, 0.01)	0.0243	(0.57, 0.00)
5348.32	Cr I	0.1450	0.0010	(0.47, 0.00)	0.0085	(0.54, 0.00)
5371.50	Fe I	0.0947	− 0.0041	(− 0.89, 0.00)	0.0063	(0.43, 0.00)
5394.67	Mn I	0.1289	− 0.0044	(− 0.90, 0.00)	0.0112	(0.71, 0.00)
5397.13	Fe I	0.1083	− 0.0053	(− 0.90, 0.00)	0.0336	(0.77, 0.00)
5405.78	Mn I	0.1089	− 0.0037	(− 0.82, 0.00)	0.0273	(0.66, 0.00)
5407.42	Mn I + Fe I	0.1545	− 0.0025	(− 0.79, 0.00)	0.0024	(0.24, 0.00)
5409.79	Cr I	0.1831	0.0021	(0.54, 0.00)	0.0038	(0.16, 0.00)
5420.35	Mn I	0.1626	− 0.0036	(− 0.82, 0.00)	0.0012	(0.22, 0.00)
5426.25	Ti I	0.0328	− 0.0007	(− 0.70, 0.00)	0.0038	(0.35, 0.00)
5429.70	Fe I	0.0997	− 0.0050	(− 0.89, 0.00)	0.0264	(0.74, 0.00)
5432.55	Mn I	0.1062	− 0.0043	(− 0.86, 0.00)	0.0092	(0.29, 0.00)
5434.53	Fe I	0.1285	− 0.0044	(− 0.87, 0.00)	0.0236	(0.70, 0.00)
5446.92	Fe I	0.1225	− 0.0054	(− 0.88, 0.00)	0.0156	(0.52, 0.00)
5455.61	Fe I	0.1289	− 0.0035	(− 0.85, 0.00)	0.0316	(0.77, 0.00)
5460.50	Ti I	0.0463	− 0.0015	(− 0.59, 0.00)	0.0022	(0.15, 0.00)
5470.63	Mn I	0.1332	− 0.0024	(− 0.72, 0.00)	0.0024	(0.39, 0.00)
5476.91	Ni I	0.2098	0.0005	(0.36, 0.00)	0.0044	(0.17, 0.00)
5483.36	Co I	0.0982	− 0.0022	(− 0.67, 0.00)	0.0018	(0.22, 0.00)
5497.52	Fe I	0.0774	− 0.0028	(− 0.78, 0.00)	0.0228	(0.71, 0.00)
5501.47	Fe I	0.1121	− 0.0014	(− 0.38, 0.00)	0.0226	(0.72, 0.00)
5506.78	Fe I	0.1167	− 0.0011	(− 0.62, 0.00)	0.0263	(0.80, 0.00)
5516.77	Mn I	0.1070	− 0.0016	(− 0.77, 0.00)	0.0010	(0.14, 0.00)
5528.41	Mg I	0.1502	− 0.0002	(− 0.06, 0.01)	0.0081	(0.43, 0.00)
5537.77	Mn I	0.1016	− 0.0027	(− 0.72, 0.00)	− 0.0039	(− 0.11, 0.00)
5569.62	Fe I	0.1612	0.0004	(0.21, 0.00)	0.0074	(0.43, 0.00)
5581.97	Ca I	0.1346	0.0009	(0.30, 0.00)	0.0072	(0.26, 0.00)
5587.86	Ni I	0.0572	− 0.0001	(− 0.23, 0.00)	0.0055	(0.22, 0.00)
5588.76	Ca I	0.1893	0.0014	(0.58, 0.00)	0.0053	(0.30, 0.00)

Downloaded from https://academic.oup.com/mnras/article-abstract/485/4/4804/5420427 by University of Hertfordshire user on 16 May 2019

Table A1 – *continued*

Centre	Species	EW	ΔEW[1]	ΔEW PCC[2]	Asym.[3]	Asym. PCC[4]
5590.12	Ca I	0.0948	0.0000	(0.21, 0.00)	0.0044	(0.35, 0.00)
5598.49	Ca I	0.0862	0.0002	(−0.09, 0.00)	0.0078	(0.26, 0.00)
5624.55	Fe I	0.1133	−0.0002	(−0.19, 0.00)	0.0170	(0.70, 0.00)
5627.64	V I	0.0703	−0.0011	(−0.56, 0.00)	0.0011	(0.22, 0.00)
5670.85	V I	0.0744	−0.0016	(−0.81, 0.00)	0.0054	(0.42, 0.00)
5703.58	V I	0.0882	−0.0011	(−0.55, 0.00)	−0.0023	(0.22, 0.00)
5707.00	V I	0.1001	−0.0014	(−0.70, 0.00)	0.0054	(0.28, 0.00)
5711.09	Mg I	0.1149	−0.0011	(−0.28, 0.00)	0.0047	(0.29, 0.00)
5782.13	Fe I	0.1319	−0.0017	(−0.63, 0.00)	−0.0017	(−0.16, 0.00)
5853.68	Ba II	0.0621	0.0009	(0.70, 0.00)	0.0034	(0.10, 0.00)
5857.45	Ca I	0.1152	−0.0001	(−0.03, 0.10)	0.0068	(0.45, 0.00)
5889.96	Na I	0.1743	−0.0046	(−0.59, 0.00)	−0.0112	(−0.13, 0.00)
5895.93	Na I	0.2286	−0.0071	(−0.69, 0.00)	0.0065	(0.15, 0.00)
6013.50	Mn I	0.1152	−0.0020	(−0.61, 0.00)	0.0100	(0.26, 0.00)
6016.64	Fe I + Mn I	0.1450	−0.0026	(−0.56, 0.00)	−0.0016	(−0.07, 0.00)
6021.80	Mn I	0.1176	−0.0000	(−0.18, 0.00)	0.0029	(0.27, 0.00)
6065.49	Fe I	0.0951	−0.0002	(−0.08, 0.00)	0.0110	(0.56, 0.00)
6081.45	V I	0.0596	−0.0013	(−0.53, 0.00)	0.0047	(0.23, 0.00)
6082.71	Fe I	0.0544	−0.0002	(−0.04, 0.04)	0.0124	(0.57, 0.00)
6085.25	Fe I + Ti I	0.0626	−0.0012	(−0.63, 0.00)	0.0046	(0.16, 0.00)
6090.21	V I	0.0699	−0.0013	(−0.59, 0.00)	0.0077	(0.52, 0.00)
6102.72	Ca I	0.2208	0.0014	(0.53, 0.00)	0.0003	(0.30, 0.00)
6111.65	V I	0.0568	−0.0013	(−0.70, 0.00)	0.0030	(0.29, 0.00)
6122.22	Ca I	0.1828	0.0004	(0.56, 0.00)	0.0078	(0.58, 0.00)
6136.62	Fe I	0.1101	−0.0010	(−0.33, 0.00)	0.0120	(0.63, 0.00)
6141.73	Ba II + Fe I	0.0576	0.0012	(0.84, 0.00)	0.0003	(0.38, 0.00)
6150.15	V I	0.0579	−0.0014	(−0.61, 0.00)	0.0028	(0.36, 0.00)
6173.34	Fe I	0.0964	0.0006	(0.48, 0.00)	0.0004	(0.23, 0.00)
6191.57	Fe I	0.1161	−0.0008	(−0.40, 0.00)	0.0081	(0.56, 0.00)
6199.19	V I + Fe II	0.0752	−0.0015	(−0.66, 0.00)	0.0028	(0.33, 0.00)
6200.32	Fe I	0.1002	0.0009	(0.48, 0.00)	−0.0038	(−0.12, 0.00)
6213.44	Fe I	0.1148	0.0015	(0.71, 0.00)	−0.0038	(0.24, 0.00)
6213.87	V I	0.0405	−0.0010	(−0.44, 0.00)	0.0065	(0.12, 0.00)
6216.36	Fe I + V I	0.0927	−0.0018	(−0.66, 0.00)	0.0074	(0.37, 0.00)
6219.29	Fe I	0.1343	0.0014	(0.54, 0.00)	0.0009	(0.08, 0.00)
6230.73	Fe I	0.2055	−0.0015	(−0.44, 0.00)	0.0096	(0.76, 0.00)
6242.83	V I	0.0566	−0.0011	(−0.56, 0.00)	0.0015	(0.17, 0.00)
6243.11	V I	0.0936	−0.0012	(−0.70, 0.00)	0.0035	(0.32, 0.00)
6246.32	Fe I	0.1655	0.0000	(0.32, 0.00)	0.0062	(0.57, 0.00)
6251.83	V I	0.0736	−0.0013	(−0.67, 0.00)	0.0013	(0.19, 0.00)
6252.56	Fe I	0.1160	−0.0002	(−0.24, 0.00)	0.0177	(0.72, 0.00)
6254.26	Fe I	0.1452	−0.0002	(0.13, 0.00)	0.0022	(−0.09, 0.00)
6256.36	Fe I + Ni I	0.1238	0.0000	(0.24, 0.00)	0.0037	(0.15, 0.00)
6265.14	Fe I	0.1207	0.0008	(0.43, 0.00)	0.0033	(0.26, 0.00)
6274.66	V I	0.0495	−0.0016	(−0.68, 0.00)	0.0029	(0.18, 0.00)
6318.03	Fe I + Ca I	0.1272	−0.0023	(−0.47, 0.00)	0.0003	(−0.19, 0.00)
6335.34	Fe I	0.1055	0.0000	(0.18, 0.00)	0.0014	(0.02, 0.26)
6358.69	Fe I	0.1259	−0.0021	(−0.28, 0.00)	−0.0040	(−0.29, 0.00)
6393.61	Fe I	0.1250	−0.0009	(−0.29, 0.00)	0.0118	(0.61, 0.00)
6400.32	Fe I	0.0820	−0.0004	(−0.34, 0.00)	0.0053	(0.42, 0.00)
6408.02	Fe I	0.1141	0.0006	(0.48, 0.00)	0.0060	(0.33, 0.00)
6421.36	Fe I	0.0891	−0.0004	(−0.22, 0.00)	0.0073	(0.47, 0.00)
6430.85	Fe I	0.1247	−0.0006	(−0.00, 1.00)	0.0034	(0.52, 0.00)
6450.20	Si I	0.1532	−0.0034	(−0.73, 0.00)	0.0056	(0.51, 0.00)
6562.80	Hα	0.7313	−0.0151	(−0.86, 0.00)	0.0027	(0.34, 0.00)
6643.64	Ni I	0.0992	−0.0015	(−0.48, 0.00)	−0.0001	(−0.02, 0.38)

This paper has been typeset from a TEX/LATEX file prepared by the author.

Downloaded from https://academic.oup.com/mnras/article-abstract/485/4/4804/5420427 by University of Hertfordshire user on 16 May 2019